

CONSTRAINING THE PROPER MOTIONS OF TWO MAGNETARS

D. L. KAPLAN^{1,2}, S. CHATTERJEE³, B. M. GAENSLER³, P. O. SLANE⁴, AND C. HALES³

Accepted for publication in the Astronomical Journal

ABSTRACT

We attempt to measure the proper motions of two magnetars — the soft gamma-ray repeater SGR 1900+14 and the anomalous X-ray pulsar 1E 2259+586 — using two epochs of *Chandra* observations separated by ~ 5 yr. We perform extensive tests using these data, archival data, and simulations to verify the accuracy of our measurements and understand their limitations. We find 90% upper limits on the proper motions of 54 mas yr^{-1} (SGR 1900+14) and 65 mas yr^{-1} (1E 2259+586), with the limits largely determined by the accuracy with which we could register the two epochs of data and by the inherent uncertainties on two-point proper motions. We translate the proper motions limits into limits on the transverse velocity using distances, and find $v_{\perp} < 1300 \text{ km s}^{-1}$ (SGR 1900+14, for a distance of 5 kpc) and $v_{\perp} < 930 \text{ km s}^{-1}$ (1E 2259+586, for a distance of 3 kpc) at 90% confidence; the range of possible distances for these objects makes a wide range of velocities possible, but it seems that the magnetars do not have uniformly high space velocities of $> 3000 \text{ km s}^{-1}$. Unfortunately, our proper motions also cannot significantly constrain the previously proposed origins of these objects in nearby supernova remnants or star clusters, limited as much by our ignorance of ages as by our proper motions.

Subject headings: astrometry — stars: pulsars: general — stars: individual: alphanumeric: (SGR 1900+14, 1E2259+58.6) — stars: neutron — X-rays: stars

1. INTRODUCTION

The sources known as magnetars (see Woods & Thompson 2006 for a review), comprised of the observational classes soft gamma-ray repeaters (SGRs) and anomalous X-ray pulsars (AXPs), are thought to be young neutron stars with magnetic fields above 10^{14} G (Duncan & Thompson 1992; Paczyński 1992). Why some neutron stars are magnetars (having magnetic field decay as their primary energy source and usually emitting no detectable radio pulsations) while others are ordinary rotation-powered radio pulsars (with comparatively little X-ray emission; Kaspi & McLaughlin 2005 and references therein) is a fundamentally unresolved issue, especially since some radio pulsars have been discovered with field strengths comparable to those of magnetars (e.g., Kaspi & McLaughlin 2005, also see Gavriil et al. 2008). The proposed explanations run the gamut from evolutionary sequences (e.g., Lin & Zhang 2004; Kasumov et al. 2006) and quiescent states (e.g., Woods & Thompson 2006; Gotthelf et al. 2004) to differences in progenitor mass (Gaensler et al. 2005) or magnetic field orientation and geometry (Zhang & Harding 2000; Kulkarni et al. 2003). Duncan & Thompson (1992) have proposed that an initial short birth period is responsible for the generation of the high magnetar fields through an efficient large scale dynamo, and have also pointed out that high magnetic fields can produce asymmetric

neutrino emission at birth, resulting in extreme space velocities ($> 10^3 \text{ km s}^{-1}$; also see Thompson & Duncan 1993, 1995; Lai 2001). Such large velocities would also help explain the apparent offsets between some SGRs and their putative natal supernova remnants (e.g., Rothschild et al. 1994). These results for magnetars, taken with the extensive investigation of rotation-powered pulsars (e.g., Ng & Romani 2007), imply that the initial spin periods, surface magnetic fields, and birth kick velocities of NS all originate in supernova core collapse processes, and the physics of these phenomena are tightly interwoven. Magnetars, by virtue of their extreme magnetic fields, may provide a direct probe of this interdependence. For example, if birth kicks are driven by asymmetric neutrino emission mediated by high B-fields (a mechanism that may not be able to produce the highest kick velocities; Lai 2001), then magnetars should have a population velocity much higher than that of the radio pulsar population. However, a more critical investigation of some of the claimed SGR/supernova remnant associations led Gaensler et al. (2001) to doubt many associations and to conclude that magnetars as a class had velocities $< 500 \text{ km s}^{-1}$, comparable to the radio pulsar population.

Such speculations were largely without concrete examination, as the velocities of magnetars are difficult to measure. As a class, they lack radio counterparts and so cannot be used for traditional Very Long Baseline Interferometry, and their spin-down properties are too noisy for measurement of “timing” proper motions. This has changed recently, though. The first measurement of the direct proper motion (and hence space velocity, with an assumed distance) of a magnetar was the work of Helfand et al. (2007), who found a proper motion of $13.5 \pm 1.0 \text{ mas yr}^{-1}$ ($\approx 212 \text{ km s}^{-1}$ at a distance of 3.5 kpc) for XTE J1810–197. This was made possible

¹ Pappalardo Fellow and Hubble Fellow; Kavli Institute for Astrophysics and Space Research and Department of Physics, Massachusetts Institute of Technology, Cambridge, MA 02139

² Current address: KITP, Kohn Hall, UCSB, Santa Barbara, CA 93106-4030; dkaplan@kitp.ucsb.edu.

³ Institute of Astronomy, School of Physics, The University of Sydney, NSW 2006, Australia; schatterjee, bgaensler@usyd.edu.au, chales@physics.usyd.edu.au

⁴ Harvard-Smithsonian Center for Astrophysics, Cambridge, MA 02138; slane@cfa.harvard.edu.

by the detection of a bright, transient radio counterpart⁵ (Halpern et al. 2005).

In this paper, we attempt to further address this issue by trying to measure the proper motions of two magnetars, SGR 1900+14 and 1E 2259+586. In the absence of steady or widespread radio counterparts, we try to measure proper motions in the X-rays: while 1E 2259+586 has an infrared counterpart (Hulleman et al. 2001) and would also be amenable to a measurement using data at those wavelengths, we try to use a technique applicable to objects without infrared counterparts, although we anticipate infrared data being used to check our measurement (Cameron, Britton, & Kulkarni 2008).

Not only can our data provide valuable constraints on the velocity distribution of magnetars, but they can also potentially address associations between the magnetars and other objects (supernova remnants and massive star clusters). Such associations are valuable for the constraints they can place on the ages, distances, and progenitor masses of magnetars (e.g., Vrba et al. 2000; Gaensler et al. 2001; Muno et al. 2006) We discuss this in more detail below.

The structure of this paper is as follows. First, in § 1.1 we discuss the two targets of this analysis, SGR 1900+14 and 1E 2259+586. We then discuss the archival data and our new *Chandra X-ray Observatory* Advanced CCD Imaging Spectrometer (ACIS; Garmire et al. 2003) observations in § 2. In § 3, we present a detailed analysis of those data, along with archival data used to test our techniques and simulations. We present our proper motion measurements in § 4, along with comparison to other similar measurements and the prospects for improvement. Finally, we give our discussion and conclusions in § 5.

1.1. SGR 1900+14 and 1E 2259+586

The third SGR discovered (Mazets, Golenetskij, & Guryan 1979), SGR 1900+14 was identified as a persistent X-ray source by Hurley et al. (1996). Subsequent observations identified the 5.2-s pulse period (Hurley et al. 1999c) with significant spin-down (Kouveliotou et al. 1999) implying a large dipolar magnetic field. The magnetar nature of this source was confirmed by the giant flare detected on 1998 August 27 (Hurley et al. 1999a; Thompson & Duncan 1995, 1996).

Vasisht et al. (1994) and Kouveliotou et al. (1994) suggested that SGR 1900+14 could be associated with the nearby supernova remnant (SNR) G42.8+0.6, based largely on position coincidence and the possible association of a number of other AXPs and SGRs with SNRs. However, Lorimer & Xilouris (2000) called the association into question when they discovered a relatively young (10^4 – 10^5 yr old) radio pulsar near both the SGR and the SNR, and Gaensler et al. (2001) calculated a 4% chance of random alignment between the SGR and SNR. This chance is even greater if one accepts that supernova explosions would naturally tend to be clustered, so SGR 1900+14 appearing near SNR G42.8+0.6 (and other SNRs; Kaplan et al. 2002) is not unlikely. If the association between SGR 1900+14 and SNR G42.8+0.6

were real, SGR 1900+14 would need a significant transverse velocity to make it from the explosion site to its current location outside the SNR’s radio shell (Hurley et al. 1999b). SGR 1900+14 is $\approx 15'$ from the center of the SNR (at approximately $\alpha_{J2000} = 19^{\text{h}}07^{\text{m}}01^{\text{s}}$, $\delta_{J2000} = +09^{\circ}04'10''$ from low-frequency radio images, with an uncertainty of $\pm 30''$; Kaplan et al. 2002). This implies a proper motion of $90\tau_{10}^{-1}$ mas yr⁻¹ or a transverse velocity $v_{\perp} \approx 2100d_5\tau_{10}^{-1}$ km s⁻¹, where the distance to the system is $5d_5$ kpc, and the age⁶ is $10\tau_{10}$ kyr. This is a large velocity for a neutron star (e.g., Hobbs et al. 2005), but not unheard of (Chatterjee et al. 2005).

An alternative association has been proposed for SGR 1900+14. Vrba et al. (2000) identified a cluster of massive stars, with several M supergiant members and > 10 other stars, about $12''$ away from the SGR 1900+14. This has been viewed as a much more secure association for SGR 1900+14, since such clusters are rarer and it is much closer on the sky, and Wachter et al. (2008) claim that the infrared ring found around SGR 1900+14 could only be powered by the cluster stars. The possible inconsistency between the extinction to SGR 1900+14 and the cluster (Kaplan et al. 2002) may not be significant, as demonstrated by Wachter et al. (2008). This cluster is at 12–15 kpc, so if the association is real then SGR 1900+14 is at a distance of $d_5 \approx 3$.

The anomalous X-ray pulsar 1E 2259+586 was the first member of its class to be discovered, when Fahlman & Gregory (1981) identified it as an X-ray point source in the center of the SNR CTB 109 that had coherent 7-s pulsations. The association with the SNR seems secure (Gaensler et al. 2001), as the positional coincidence is very good ($< 3'$) compared to the local density of SNRs. Based on interactions between the SNR and H II regions with measured distances, Kothes, Uyaniker, & Yar (2002) find a distance⁷ of ≈ 3 kpc.

2. OBSERVATIONS

We examined the *Chandra* archive for suitable observations of magnetars. We found data on SGR 1900+14 and 1E 2259+586 that we used for the first epochs of our proper motions studies. These data were taken with the ACIS instrument in the full-frame mode and with no grating, in contrast to many other observations of magnetars that use subarrays, continuous clocking, or gratings to get better timing or spectral resolution.

We re-observed SGR 1900+14 and 1E 2259+586 with *Chandra*, with the new data serving as second epoch observations to try to measure or constrain their proper motions. For the second epochs, we chose to generally replicate the first epochs in detector choice, aim-point, and exposure time. One of the priorities was

⁶ Both the age and distance of the SGR 1900+14 are highly uncertain. The spin-down age $P/2\dot{P}$ is about 1 kyr, but the spin-down rates of magnetars can easily vary by factors of several (Woods & Thompson 2006), thus making the spin-down age an unreliable estimator of the true age. The distance to SGR 1900+14 itself is largely unconstrained.

⁷ There is some uncertainty about the association and hence the distance to 1E 2259+586. Durant & van Kerkwijk (2006) find a distance to 1E 2259+586 of 7.5 ± 1.0 kpc using the “red clump” method. They argue that CTB 109 could also plausibly be at this distance too, based on a reinterpretation of radial velocity data, but there are uncertainties associated with this analysis.

⁵ Helfand et al. (2007) also used infrared measurements of XTE J1810–197 to constrain the proper motion, and found a much coarser but consistent result.

TABLE 1
 SUMMARY OF *Chandra* OBSERVATIONS

Target	Epoch	ObsID	Date	MJD	Aimpoint	Exposure (ksec)	Rotation (deg)
SGR 1900+14	1	1954	2001-Jun-17	52077	ACIS-I	29.8	148.6
	2	6731	2006-Jun-04	53891	ACIS-I	24.6	134.0
1E 2259+586	1	725	2000-Jan-12	51555	ACIS-S	18.9	312.8
	2	6730	2006-May-09	53864	ACIS-S	24.8	73.7

NOTE. — The rotation given is the nominal roll angle of the spacecraft, defined by the `ROLL_NOM` header keyword.

to detect as many other sources as possible besides the SGR 1900+14/1E 2259+586: as discussed below, our accuracy is limited by the number and quality of the reference sources. In Table 1 we give the details of both the archival observations and our new ones. Note that the rotations of the new and old observations are in general different. For SGR 1900+14, which used the square ACIS-I detector, this made no difference, but for 1E 2259+586 the reference sources changed somewhat between epochs, giving us a smaller set than we would have liked: see discussion in § 4.2.

3. X-RAY ASTROMETRY

Our general analysis technique is to (1) measure the positions of a number of field X-ray sources (“reference sources”) common to both epochs; (2) measure the position of the object of interest (SGR 1900+14 or 1E 2259+586) in both epochs; (3) use the reference sources to determine a transformation between the two observations; and (4) apply that transformation to the object of interest, finding the position difference (if any) between the two epochs that we can then convert to a proper motion. This generally echoes the techniques of Hui & Becker (2006), Winkler & Petre (2007), and Motch et al. (2007a,b), although like Motch et al. (2007a,b) we prefer to use many reference sources and not just a few.

We must determine the best way to carry out each step, and assess the uncertainties associated with each. For this reason, we discuss each step at length below, in many cases using data from other observations and/or simulations to assess accuracy.

In the discussion below, we work as much as possible in the sky pixel ($x_{\text{sky}}, y_{\text{sky}}$) frame. This is a frame constructed by the *Chandra* event processing that rotates the detector ($x_{\text{det}}, y_{\text{det}}$) frame to have y_{sky} pointing north and x_{sky} pointing west. While in general we prefer to stay in a frame with as little processing as possible, which would argue for retaining the detector frame, the continuous dither of *Chandra* (in a Lissajous pattern with amplitude $\pm 8''$ and periods of 707 s and 1000 s along the two axes) makes that difficult. The conversion from detector to sky frame involves correcting for that dither, for the nominal orientation of the spacecraft, and for any other position excursions, but this aspect reconstruction is of sufficient quality that it does not limit our accuracy.

3.1. Reference Sources

For our main position-finding algorithm, we chose the CIAO task `wavdetect` (Freeman et al. 2002), which uses a wavelet-based detection algorithm. This echoes the choices made by such large X-ray surveys as the

Chandra Multiwavelength Plane (ChaMPPlane) Survey (Hong et al. 2005) and the *Chandra* Multiwavelength Project (ChaMP; Kim et al. 2007). In those cases the algorithm choice was made for optimum source detection, with astrometry only as a secondary goal, but they did find that `wavdetect` produced the most reliable astrometry. We verified this choice by comparing the results of `wavdetect`, the sliding-cell task `celldetect`, and our own implementation of an interactive centroiding task that operates on the raw event lists, and found that `wavdetect` gave the smallest scatter in the various tests described below.

As we were not overly concerned with detecting every possible source or measuring such source properties as count-rate, we ran `wavdetect` on the raw level 2 event files returned from the *Chandra* archive without any additional processing (e.g., exposure map creation), using wavelet scales of 1, 2, 4, 8 pixels. We did test whether removing sub-pixel randomization⁸ made a difference in the positions, and we find no systematic difference.

However, the uncertainties reported by `wavdetect` are systematically low, especially for off-axis sources. We therefore investigated the uncertainty models used by the ChaMP and ChaMPPlane projects. Independent of the analyses of Hong et al. (2005) and Kim et al. (2007), which relied on `MARX` (Model of AXAF Response to X-rays) and `SAOSAC` (a raytracing code developed for *Chandra*) simulations of sources, we wished to see how reliable the position measurement and uncertainty estimation of `wavdetect` are. Therefore we took a number of relatively long ACIS-I exposures from the archive with a large number of point sources. We then split those exposures into two halves by time, effectively making two sub-exposures that are otherwise identical, and processed each with `wavdetect` in the same manner. This way we can examine how the positions from the first half agree with those from the second half: since the two sub-exposures are from the same observation, the positions should agree. Of course the sources in each sub-exposure will have fewer counts than the sources in the total exposure, but there are still a range of count levels and off-axis angles.

We first did this comparing the results of `wavdetect` with `celldetect` and an interactive centroiding algorithm that we implemented, and found `wavdetect` to have the lowest dispersion. We then varied the energy range of our source extraction and found that including event energies from 0.3 keV to 7 keV optimized the signal-to-noise of the extraction.

We then compared the position differences between the first and second sub-exposures with the position

⁸ See <http://cxc.harvard.edu/ciao/threads/acispixrand/>.

uncertainties returned by `wavdetect`. We found that `wavdetect` significantly underestimated the uncertainties, especially at off-axis angles $\theta > 3.5'$. The comparison gave a reduced χ^2 of 4.31 for 1450 degrees-of-freedom (DOF), and the shape of the distribution is clearly broader than the expected distribution, with more points at $> 2\sigma$. In contrast, both the ChaMP and ChaMPlane models work well, giving reduced χ^2 values of 1.33 and 1.02. The uncertainty from the ChaMPlane model exceeds that from the ChaMP model slightly at large and small off-axis angles, leading to the slightly lower χ^2 for ChaMPlane.

Overall, both the ChaMP and ChaMPlane uncertainty models appear to work. Both are based on simulations using MARX, and so the agreement is not surprising, but since they agree with each other and also agree with the actual data presented here (see § 3.4) we feel comfortable using either. The functional form of the ChaMP model is somewhat simpler and conforms more to the expected relation between uncertainty $\sigma_{x,y}$ and signal-to-noise ratio, with $\sigma_{x,y} \propto C^{-0.46}$ (C is the number of counts above the background) compared to the expected $\sigma_{x,y} \propto C^{-0.5}$ (i.e. $\sigma_{x,y} \propto (S/N)^{-1/2}$). In contrast, the ChaMPlane model is a more complicated function of C involving powers of the logarithm of C . Therefore we will use the ChaMP model (see eq. 14 of Kim et al. 2007):

$$\sigma_{x,y} = 0.77 C^{-0.46} 10^{0.11\theta} \text{ pixels} \quad (1)$$

with $\sigma_{x,y}$ as the x or y uncertainty (converted from the radial uncertainty in Kim et al. 2007 by dividing by 1.515; see Lampton, Margon, & Bowyer 1976), and θ in arcminutes. Note that this is only valid for low count levels ($C < 131$) as is the case here but not for SGR 1900+14 or 1E 2259+586.

3.2. SGR 1900+14

For SGR 1900+14, we are in a very different regime than for the reference sources. Instead of relatively faint sources at a variety of off-axis angles, we have a bright source at $\theta < 0.5'$. A different approach to position measurement and uncertainties than that described in § 3.1 is needed.

The ACIS-I images of SGR 1900+14 have the source at an off-axis angle of $20''$, and with about 5000 counts. Technically, then, the ChaMP uncertainty models do not apply (they are only valid for < 2000 counts). Even so, the ChaMP model for high numbers of counts does not agree with what we would naively expect, with $\sigma_{x,y} \propto C^{-0.2}$. We therefore did our own SAOSac/MARX (using the *Chandra* Ray Tracer ChaRT as an interface to the SAOSac raytracing code; Carter et al. 2003) simulations of this source.

We simulated a bright point-source at the correct off-axis location with the approximate spectrum of SGR 1900+14: a power-law with photon index $\Gamma = 1.9$ and absorption with $N_{\text{H}} = 2 \times 10^{22} \text{ cm}^{-2}$ (Mereghetti et al. 2006). We simulated a source with 700,000 counts, many more counts than are actually detected in our exposures of SGR 1900+14, so that we could divide this exposure into sub-exposures as above for comparison. We made a series of sub-exposures, dividing the 700,000 total counts into 12 sub-exposures with 56,000 counts, 25 sub-exposures with 27,000 counts,

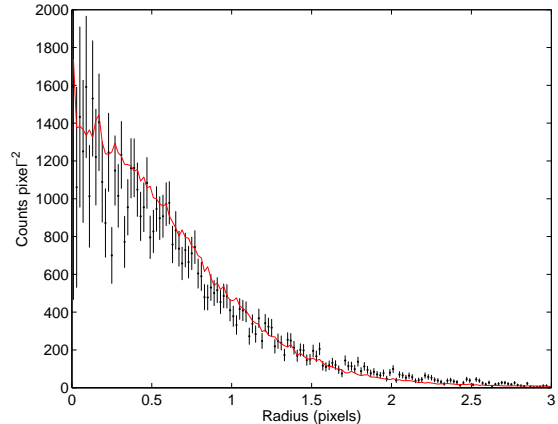


FIG. 1.— Radial profile of SGR 1900+14 (points) compared to that of a MARX simulation with 30 times the number of counts (solid line) that does not include the effects of pileup. The agreement between the data and the model illustrates the small effect of pileup on the radial profile of SGR 1900+14.

and so on, down to 300 sub-exposures with 2200 counts. We then ran `wavdetect` on each of the sub-exposures in a series and compared all of the positions. In contrast to the situation with the reference sources, where the raw `wavdetect` uncertainties underpredicted the uncertainties, here they did well. In all cases the comparisons yielded reduced χ^2 values consistent with 1.0. Fitting the uncertainty as a function of number of counts, we find a relation close to the expected one, with $\sigma_{x,y} \propto C^{-0.47}$.

To confirm this, we also divided up the real exposures of SGR 1900+14 into 10 sub-exposures of ≈ 500 counts each. Each position as measured by `wavdetect` had an uncertainty of 0.04 pixels, and again the positions of the sub-exposures were all consistent with each other within the uncertainties.

A final concern is pileup. With a count-rate of $\sim 0.17 \text{ s}^{-1}$, the expected pileup fraction is $\sim 20\%$, with ~ 0.5 event expected in each 3.2 s frame. This means that our data are affected by pileup such that spectral estimation will not be robust, but at this pileup level the effect on astrometry is minimal. The spatial distribution of events is still largely consistent with the point-spread function (Fig. 1). Our MARX simulations here did not account for pileup, but even so they were consistent with our examination of the sub-exposures of the real data. Overall, then, `wavdetect` positions and uncertainties seem sufficient for observations of SGR 1900+14.

3.3. 1E 2259+586

For 1E 2259+586, we could not use the results of `wavdetect`. The pileup for this source is severe enough that the X-ray image has a central hole, where so many X-ray photons landed that all were judged to be cosmic rays. We also have issues at large radii: beyond a radius of $\approx 4''$, there is extended emission from a combination of the SNR in which 1E 2259+586 is embedded, as well as a halo from dust scattering (Patel et al. 2001).

We initially tried doing simple centroids on the event data, where we used events in an annulus whose inner radius varied from 0 to 5 pix (to eliminate the central hole) and whose outer radius varied from 15 pix to 100 pix. For data with no central hole, iterating this process will converge on the correct center (this was one of the methods we used in § 3.2). However, we found that this method

TABLE 2
 SOURCE POSITIONS FOR SGR 1900+14

ID	Epoch 1				Epoch 2			
	x_{sky}	y_{sky}	Counts	θ (arcmin)	x_{sky}	y_{sky}	Counts	θ (arcmin)
X	4075.5 ± 0.0	4067.4 ± 0.0	5232.3	0.3	4109.7 ± 0.0	4022.9 ± 0.0	3805.6	0.3
1	3991.4 ± 0.5	4425.6 ± 0.5	15.5	2.8	4025.8 ± 0.5	4380.5 ± 0.5	11.7	2.8
2	4080.5 ± 0.4	4494.6 ± 0.4	30.5	3.3	4114.7 ± 0.6	4448.8 ± 0.6	12.7	3.2
3	4159.6 ± 1.0	4707.2 ± 1.0	10.5	5.0	4192.8 ± 1.1	4662.8 ± 1.1	8.1	5.0
4	4385.9 ± 0.4	4822.8 ± 0.4	138.2	6.4	4419.6 ± 0.5	4779.3 ± 0.5	95.3	6.4
5	4409.6 ± 0.7	4421.9 ± 0.7	9.6	3.7	4442.6 ± 1.3	4378.2 ± 1.3	2.9	3.7
6	4025.4 ± 1.5	4785.1 ± 1.5	6.3	5.7	4059.5 ± 1.0	4743.5 ± 1.0	15.8	5.7
7	4383.0 ± 1.7	4655.8 ± 1.7	3.5	5.2	4418.8 ± 1.4	4612.8 ± 1.4	5.7	5.2
8	4395.0 ± 1.9	5093.7 ± 1.9	18.6	8.5	4425.4 ± 2.3	5053.4 ± 2.3	12.5	8.6
9	3638.7 ± 0.6	4492.5 ± 0.6	29.0	5.0	3674.1 ± 0.8	4446.7 ± 0.8	15.8	4.9
10	3997.8 ± 0.5	4280.2 ± 0.5	5.7	1.7	4032.3 ± 0.5	4235.4 ± 0.5	6.8	1.7
11	3055.8 ± 1.9	4475.3 ± 1.9	23.9	9.1	3090.0 ± 1.9	4426.7 ± 1.9	24.1	9.0
12	3112.3 ± 1.0	4680.9 ± 1.0	128.4	9.4	3148.0 ± 2.0	4635.6 ± 2.0	24.8	9.3
13	3319.6 ± 1.3	4314.9 ± 1.3	13.8	6.6	3355.5 ± 1.2	4270.0 ± 1.2	16.7	6.5
14	4313.9 ± 0.4	4043.5 ± 0.4	9.7	1.8	4348.5 ± 0.5	3999.2 ± 0.5	7.7	1.9
15	4398.5 ± 0.6	4043.0 ± 0.6	7.7	2.5	4433.8 ± 0.7	3998.2 ± 0.7	5.8	2.6
16	4706.4 ± 0.9	3894.6 ± 0.9	14.0	5.3	4739.4 ± 1.1	3848.5 ± 1.1	8.9	5.3
17	4781.0 ± 0.7	3963.5 ± 0.7	35.0	5.7	4814.3 ± 1.0	3918.2 ± 1.0	15.3	5.8
18	4694.9 ± 1.1	4248.4 ± 1.1	9.1	5.1	4730.5 ± 1.0	4200.2 ± 1.0	10.1	5.1
19	3839.5 ± 0.6	3917.6 ± 0.6	7.7	2.6	3873.1 ± 0.5	3872.6 ± 0.5	10.9	2.5
20	3931.1 ± 0.5	3957.6 ± 0.5	8.7	1.8	3965.4 ± 0.4	3912.9 ± 0.4	9.8	1.7
21	4005.7 ± 0.4	3945.3 ± 0.4	8.6	1.4	4040.1 ± 0.4	3900.6 ± 0.4	8.7	1.4
22	4046.3 ± 0.3	3940.9 ± 0.3	13.6	1.3	4080.3 ± 0.5	3896.7 ± 0.5	5.8	1.3
23	3582.5 ± 0.9	3748.2 ± 0.9	12.9	5.1	3617.3 ± 1.0	3703.3 ± 1.0	10.4	5.0
24	3925.2 ± 1.1	3545.0 ± 1.1	7.4	4.7	3958.9 ± 0.8	3499.8 ± 0.8	13.9	4.7
25	4125.5 ± 1.0	3069.3 ± 1.0	72.4	8.4	4158.6 ± 1.1	3024.0 ± 1.1	53.8	8.5
26	4207.8 ± 1.4	3368.5 ± 1.4	8.5	6.0	4241.9 ± 1.0	3323.4 ± 1.0	16.3	6.1
27	4255.9 ± 0.9	3715.3 ± 0.9	4.8	3.4	4289.4 ± 0.7	3670.6 ± 0.7	7.8	3.4

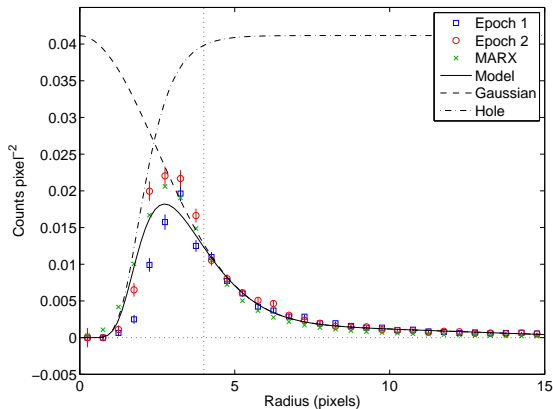
 NOTE. — Positions are in sky pixel coordinates, θ is the off-axis angle, and source X is SGR 1900+14.


FIG. 2.— Radial profiles of 1E 2259+586 (squares and circles for epochs 1 and 2) compared to that of a MARX simulation that includes pileup (x’s). We fit the data outside of a radius of 4 pix (vertical dotted line) with a Gaussian (dashed line) multiplied by a hole (dot-dashed line; the hole has the form $\tanh(r/r_0)^{10}$ with $r_0 = 1.25$ pix); the full model is the solid line.

gave results that did not converge: changing the outer radius led to systematic changes in the centroid position. This was partially due to asymmetries in the extended X-ray emission, but more important were the effects of non-uniform exposure over the ACIS CCDs. Together, these effects led to variations (both smooth and discrete) of the overall count level over the image, and when the annuli that we chose included those portions, they skewed the resulting centroid. Simulating the data in MARX, where we used similar exposure maps, reproduced the wandering centroid, although not to a high enough precision that the MARX data would allow us to correct the observations.

Instead, we followed Hulleman et al. (2001) and ex-

PLICITLY used a local, symmetric function to find the position of 1E 2259+586. This is similar to what we did with SGR 1900+14, where `wavdetect` found the position that maximized the overlap between the data and a wavelet function, but for 1E 2259+586 we use our own kernel function and our own routines to find the position. For the kernel we used a Gaussian function multiplied by a hole, meant to mimic the shape of the piled-up image. The function was radially symmetric. Hulleman et al. (2001) used a hyperbolic tangent for their “hole” function: we found that this did not decline quite quickly enough to match our data, and instead used $\tanh(r/r_0)^{10}$, where r_0 is the radius scale and the exponent serves to increase the sharpness of the hole; the results are not sensitive to the exponent as long as it is $\gtrsim 4$. A fit to the data from both epochs (averaged in azimuth), along with a MARX simulation that includes pileup, is shown in Figure 2. To make that fit, we fit the Gaussian to the data, the MARX model with pileup, and the MARX model without pileup, all for radii of ≥ 4 pix. At those radii the data and the two models all agree reasonably well. Within 4 pix the effects of pileup become more severe, and the MARX model is not able to accurately predict the data, but the agreement is qualitatively reasonable. We found a hole radius $r_0 \approx 1.25$ pix, but again the fit was not extremely sensitive to this value. The goal of this model is to give a good qualitative representation of the data, not to fit it in great detail.

To actually find the position of 1E 2259+586, instead of fitting the data, which is sensitive to the details of the model as well, we prefer to cross-correlate a fixed model

TABLE 3
SOURCE POSITIONS FOR 1E 2259+586

ID	Epoch 1				Epoch 2			
	x_{sky}	y_{sky}	Counts	θ (arcmin)	x_{sky}	y_{sky}	Counts	θ (arcmin)
Y	4141.7 ± 0.1	4171.9 ± 0.1	...	0.7	4117.0 ± 0.1	4070.7 ± 0.1	...	0.3
1	4093.8 ± 0.4	3567.5 ± 0.4	64.6	4.3	4069.9 ± 0.3	3466.8 ± 0.3	157.7	5.2
2	4536.1 ± 0.2	3899.2 ± 0.2	295.7	4.0	4510.9 ± 0.5	3798.9 ± 0.5	26.6	4.2
3	4159.5 ± 0.3	3799.6 ± 0.3	38.7	2.5	4135.0 ± 0.4	3699.7 ± 0.4	21.6	3.3
4	4270.1 ± 0.2	4755.3 ± 0.2	330.9	5.6	4245.3 ± 0.3	4654.4 ± 0.3	103.4	4.7
5	4350.6 ± 0.4	4446.1 ± 0.4	28.9	3.5	4326.3 ± 0.3	4344.7 ± 0.3	47.6	2.8
6	4273.3 ± 1.2	4961.5 ± 1.2	24.4	7.2	4246.7 ± 1.0	4857.9 ± 1.0	20.8	6.4

NOTE. — Positions are in sky pixel coordinates, θ is the off-axis angle, and source Y is 1E 2259+586.

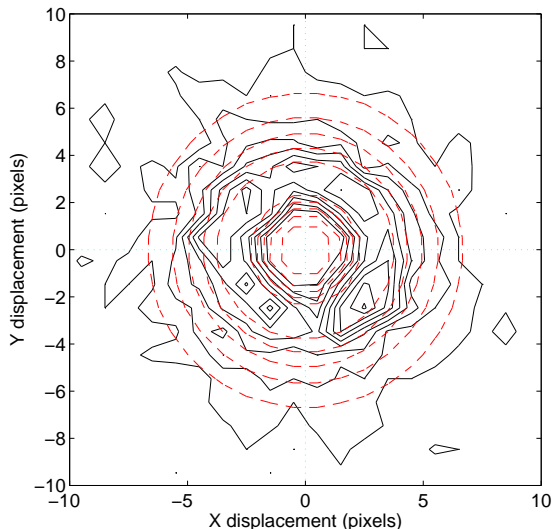


FIG. 3.— Cross-correlation of the first epoch of data for 1E 2259+586 (black solid contours) with the model from Eqn. 2 (red dashed contours). The model and data have been shifted to the origin based on the result of the cross-correlation. The results for epoch 2 are similar.

with the data. Our fixed model is that shown in Figure 2:

$$F(r) = e^{-r^2/2\sigma^2} \tanh^{10} \left(\frac{r}{r_0} \right) \quad (2)$$

where we found $\sigma = 2.5$ pixels and $r_0 = 1.25$ pixels gave good results. This function is radially symmetric, and by cross-correlating rather than fitting we can ignore issues of normalization and the variations in the wings of the radial profile. Above, we could have just fit the data to a Gaussian function only for radii greater than 4 pixels, but this would not have allowed the cross-correlation. Using a Gaussian kernel function with no hole but just excluding a portion of the data performed poorly, since the sharp “horns” of the data outside of the hole can cause local maxima in the cross correlation if the kernel function has a single peak like a Gaussian.

We cross-correlated images of the filtered event files created from both the data and the MARX simulations with the model (Fig. 3). The cross-correlation results were smooth and well-behaved, and we interpolated between our grid points to find the best-fit offset. We made sure that the fitted position did not depend on the details of the cross-correlation: we varied the binning, the outer radius, and the parameters of the model (σ and r_0), and in all cases the resulting variations in the position were < 0.05 pix. As a further check, we shifted the event

positions by random amounts of up to 1 pix, and found that we were able to recover the shifts to an accuracy of < 0.1 pix; this test also verified that our result did not depend on the origin of the binning. Based on these tests, as well as additional MARX simulations, we estimate that our cross-correlation is accurate to ± 0.1 pix in each coordinate.

As another test, we also cross-correlated the binned images from epochs 1 and 2 against each other, rather than against a smooth kernel. In general the results of this test were similar, where we could recover an input shift at a level of < 0.1 pix, and the offsets agreed to a similar precision. We plot the results of all cross-correlations (epoch 1 vs. model, epoch 2 vs. model, and epoch 1 vs. epoch 2) in Figure 4, where we plot the results relative to the best-fit positions given in Table 3. The cross-correlations that we plot do not agree exactly with the positions in Table 3 as those positions were derived using multiple cross-correlations with random offsets used to eliminate the effects of binning, but the agreement is better than the quoted ± 0.1 pix uncertainty.

For a final check, we examined the position of the readout streak on the two epochs. This streak comes about because the ACIS detector has no shutter, so the CCDs receive photons even as the charge is being clocked off. This gives rise to a one-dimensional streak centered on each bright source which is aligned with the CCD row and column axes. It ends up having $\sim 2\%$ of the total number of events as the original source⁹, and can be used for both positional and spectral information. Here we make use of only the former.

To use the streak, we took the event positions from the level-2 event file. We then rotated by the `ROLL_NOM` header keyword, putting them into a frame where the CCD rows and columns were vertical and horizontal (similar to the `CHIP` frame). The readout streak, which is a line in the sky (x, y) frame not aligned with either axis, is now horizontal. We then stepped along the line, computing the median event position in the vertical direction: see Figure 5. For both epochs 1 and 2, we found streak positions that were consistent to ± 0.02 pix with our best-fit positions of 1E 2259+586 from Table 3, albeit in one dimension. While not sufficient to get a position for 1E 2259+586 alone, this provides additional confirmation that our cross-correlation technique is accurate to the claimed 0.1 pix.

⁹ See http://cxc.harvard.edu/cal/Acis/Cal_prods/xfer_streak/index.htm

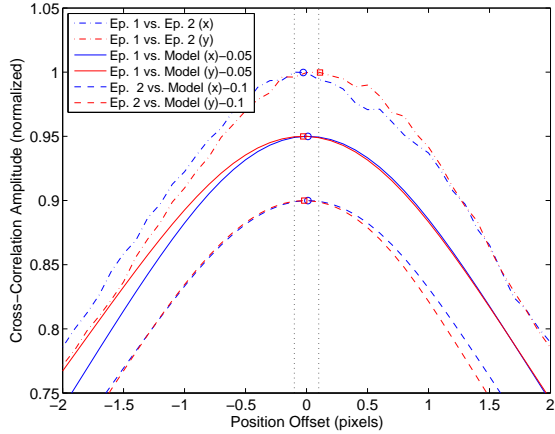


FIG. 4.— Cross-correlation results for 1E 2259+586. We show one-dimensional cuts through the peak of the cross-correlation surface, which we use to identify the best-fit positions in x (blue curves) and y (red curves). For each cross-correlation (epoch 1 vs. epoch 2: dot-dashed line; epoch 1 vs. the model: solid line; epoch 2 vs. the model: dashed line; in all cases the model is from Eqn. 2) we interpolated to find the maximum value of the cross-correlation, which we identify as the best-fit position, and the cross-correlations have been offset vertically for clarity. The data plotted here have had our nominal positions subtracted, giving offsets near 0. They are not quite at zero as the nominal positions were the averages of cross-correlations done with a range of random offsets added to mitigate the effects of binning, but the differences are consistent with our claimed uncertainty of 0.1 pix (vertical dotted lines).

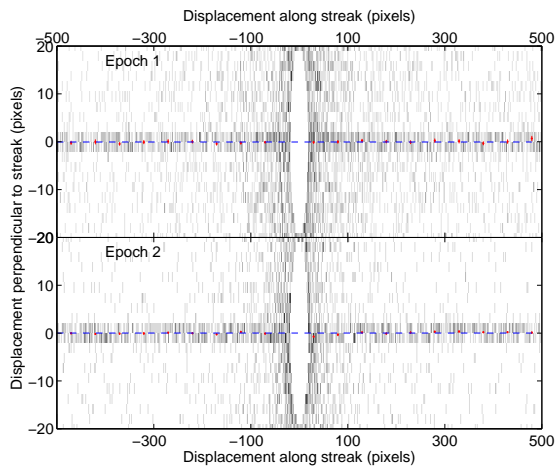


FIG. 5.— Fits to the readout streak of 1E 2259+586: epoch 1 (*top*) and epoch 2 (*bottom*). We rotated the event locations according to the `ROLLNOM` header keyword, ending up in a frame where the CCD readout streak was horizontal. The grayscales are the binned images for each epoch; the bins appear rectangular in this plot because of the drastically different scales for the ordinates and abscissae. We then constructed 50 pixel wide bins along the streak and computed the median event locations perpendicular to the streak, which we show as the points. The dashed lines are the averages of the median positions. We have excluded events within a radius of 20 pix around 1E 2259+586.

3.4. Frame Transformations

We considered a number of ways to transform between the position measurements at each stage. To test this, we used 13 ACIS-I observations¹⁰ of the Hubble Deep Field North (HDF-N; Hornschemeier et al. 2000 and subsequent papers). The observations were between 50 ks and 140 ks in depth, and detected > 100 sources. Note

¹⁰ We used ObsIDs: 2232, 2233, 2234, 2421, 2423, 3293, 3294, 3388, 3389, 3390, 3391, 3408, and 3409.

that the observational setup here was, if anything, more taxing than what we used for our proper motion observations. This was because a number of the observations had a different aimpoint (off by about half of an ACIS detector) and varying roll angles. We identified 38 sources that were common to each exposure (note that this was not a completely exhaustive search, but comprised those that we could identify easily) and computed transformations between each pair of observations. We used a number of different transformations with different levels of complexity.

2-parameter : A shift in x and y .

3-parameter : A shift in x and y , along with a rotation.

4-parameter : A shift in x and y , along with a rotation and an overall scaling.

6-parameter : A general linear transformation, involving a shift and a separate rotation and scaling for each axis (e.g., see Eqn. A5 in Kaplan, van Kerkwijk, & Anderson 2007).

We were transforming between x and y values in the SKY frame, so the nominal position angle of *Chandra* was already taken out. Any remaining rotation or scaling would account for imprecise knowledge of the spacecraft’s orientation and breathing of the ACIS-I detector (changes in the plate-scale due to thermal variations), respectively.

Overall we found that the 3-parameter transformation provided a significant decrease in χ^2 compared to the 2-parameter transformation, with a mean $\Delta\chi^2$ of 23.8 going from 74 to 73 DOF. This is extremely significant, with an F-test probability of $< 10^{-5}$ that this is due to chance. Therefore a non-zero rotation is required between different observations, with a magnitude of $\approx 0.05^\circ$. Comparing sets of three observations, the rotations ϕ fitted between all of them are consistent, with (e.g.,) $\phi(1 \rightarrow 2) + \phi(2 \rightarrow 3) \approx \phi(1 \rightarrow 3)$, indicating that the rotations can be physically meaningful. With just the 3-parameter transformation the reduced χ^2 was consistent with 1.0, and the distribution of position residuals was consistent with the expected distribution (Fig. 6). This indicates that our uncertainty model is reasonable: tests using the `ChaMPlane` model gave similar results, while those using the raw `wavdetect` uncertainties had reduced χ^2 larger than 2. Beyond this, the more complicated transformations were not warranted, with a median $\Delta\chi^2$ of only 4.2 between 3 parameters and 6.

4. MEASURING PROPER MOTIONS

4.1. SGR 1900+14

To actually measure the proper motion of SGR 1900+14, first we ran `wavdetect` on both observations. The parameters were the same as those discussed in § 3. We then identified sources common to both epochs of the data, finding 27 sources in addition to SGR 1900+14. These sources were on all four of the ACIS-I CCDs. It would be preferable to have the SGR 1900+14 centered on a single CCD, and to only use sources on that detector. That way we would not have to worry about inaccuracies in the relative positions of the detectors or shifts in their positions with time

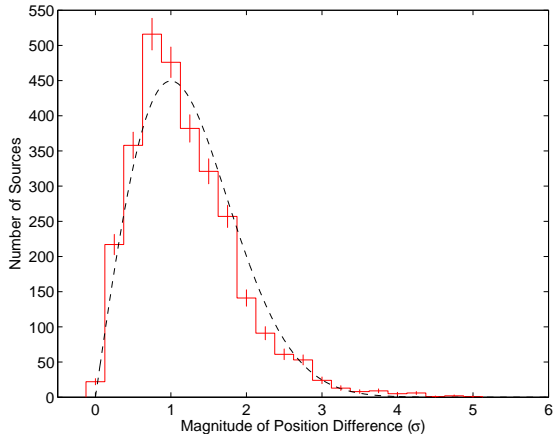


FIG. 6.— Position differences for 2964 sources compared between different observations of the HDF-N (38 unique sources and 78 pairs of observations), normalized by position uncertainty (computed according to Eqn. 1). The data are the histogram, and we also show the expected distribution with $N(r) \propto re^{-r^2/2}$ for comparison.

affecting our astrometry. However, that would severely restrict our field of view, and we felt that the gain of additional reference sources outweighed the possibility of smaller uncertainties for the detected sources. The various tests and discussion in § 3.1 seem to indicate that using sources on different CCDs does not adversely affect our astrometry, at least at the level considered here.

With the source detections, we then updated the position uncertainties of all of the sources except SGR 1900+14 using Eqn. 1. Finally, we fit for the transformation between the two epochs of data, using a 3-parameter fit (§ 3.4). The data gave a very good fit, with $\chi^2 = 37.7$ for 51 DOF (27 reference sources and 3 parameters). There were no significant outliers in the data, which is not really surprising since we only included sources that we could match initially between the epochs. The magnitude of the residuals is $\sim 100 \text{ mas yr}^{-1}$, which is far larger than the proper motion one would expect from random field stars (i.e., at 1 kpc 100 mas yr^{-1} is 475 km s^{-1} , which is much larger than the velocity dispersion of Galactic stars). Therefore we can consider that we are measuring the motion of SGR 1900+14 relative to reference stars that are at rest. Similarly, corrections for Galactic rotation and Solar motion are too small to be considered.

The fitted rotation here was consistent with 0. We therefore found that a 2-parameter transformation was sufficient (with virtually no change in χ^2), and with the smaller number of free parameters the resulting position difference had smaller uncertainties. While in § 3.4 we found that a rotation was necessary, here we do not, although whether it is the simpler observational setup (both observations had the same aimpoint, in contrast to § 3.4) or just the reduced accuracy from a smaller number of reference sources that changed the situation we do not know. We plot the residual position differences of the reference sources in Figure 7.

As a check on our transformation, we performed jackknife tests, where we calculate the transformation for the data excluding a single reference source (see, e.g., Efron & Tibshirani 1993). This tests whether or not the transformation depends overly on a single reference

source, and indeed we find that it does not. We find that the means of the jackknifed shifts are consistent with the value using all of the data, and that the standard deviations are significantly less than our estimated shift uncertainties. We then performed a bootstrap test. Here we created 100 data sets, each including a random subset chosen with replacement from the 27 reference sources. The resulting shifts are again distributed around the proper values created from the actual data, and the standard deviations are comparable to our uncertainties (they are actually slightly smaller). Based on these two tests, we see that our transformation calculation is reasonably robust to choices of the input data.

With the 3-parameter transformation, we find that the position of SGR 1900+14 is consistent between the two epochs, moving by 0.27 ± 0.27 pixels, implying no measurable proper motion. Note that the bulk of this uncertainty comes from uncertainties in the fitted transformation (uncertainties in each coordinate of the shift of 0.26 pixels, and an uncertainty in the rotation of 0.03°), since the individual position measurements of SGR 1900+14 had uncertainties of < 0.02 pixels. We also checked to see if the choice of transformation (2, 3, 4, or 6 parameters), uncertainty model (ChAMP or ChAMPlane), or level of processing (with or without ACIS randomization) made a difference, and find that all of the results were consistent. With the 2-parameter transformation, which as discussed above is sufficient, we find a very similar shift but smaller residuals: $(\Delta x, \Delta y) = (0.02 \pm 0.19, 0.26 \pm 0.19)$ pixels, or a magnitude 0.27 ± 0.19 pixels for the 2-parameter fit. Again, the uncertainties are dominated by the 0.18 pixel uncertainties in each coordinate of the shift. We give the detailed fit results in Table 4.

The interval between the observations was $\Delta t = 1813.3 \text{ days} = 4.96 \text{ yr}$, so we have a proper motion in pixels $(\mu_x, \mu_y) = (2.4 \pm 18.4, 26.3 \pm 18.4) \text{ mas yr}^{-1}$. The celestial proper motion is $(\mu_\alpha, \mu_\delta) = 0'.492(-\mu_x, \mu_y)$, which is $(\mu_\alpha, \mu_\delta) = (-2.4 \pm 18.4, 26.3 \pm 18.4) \text{ mas yr}^{-1}$. If we actually want to limit the speed of SGR 1900+14, we can look at the distribution of the magnitude $\mu = \sqrt{\mu_x^2 + \mu_y^2}$. Our measurements were $\mu_x = \hat{\mu}_x \pm \sigma_{\mu,x}$ and $\mu_y = \hat{\mu}_y \pm \sigma_{\mu,y}$, although $\sigma_{\mu,x} = \sigma_{\mu,y} = \sigma_\mu$. If we look at the magnitude of the proper motion $\mu = \hat{\mu} \pm \sigma_\mu$, where $\hat{\mu} = \sqrt{\hat{\mu}_x^2 + \hat{\mu}_y^2}$, the probability density function for μ is:

$$f_\mu(\mu) = \left(\frac{\mu}{\sigma_\mu^2}\right) I_0\left(\frac{\mu \hat{\mu}}{\sigma_\mu^2}\right) e^{-(\mu^2 + \hat{\mu}^2)/2\sigma_\mu^2}, \quad (3)$$

where $I_0(x)$ is the modified Bessel function of the first kind (Papoulis 1991, p. 140). From numerical integration, we find that the mean, mode, and median are all close to each other. For SGR 1900+14, the mean is 33 mas yr^{-1} (vs. $\hat{\mu} = 26 \text{ mas yr}^{-1}$), and we find a 90% upper limit to μ to be 54 mas yr^{-1} , or a transverse velocity $v_\perp < 1300 d_5 \text{ km s}^{-1}$.

4.2. 1E 2259+586

We followed the same procedure as for SGR 1900+14 above to find the reference sources for 1E 2259+586. Here, though, we could only identify 6 sources common to both epochs (a seventh source was identified, but it is right near the gap between detectors and the positions

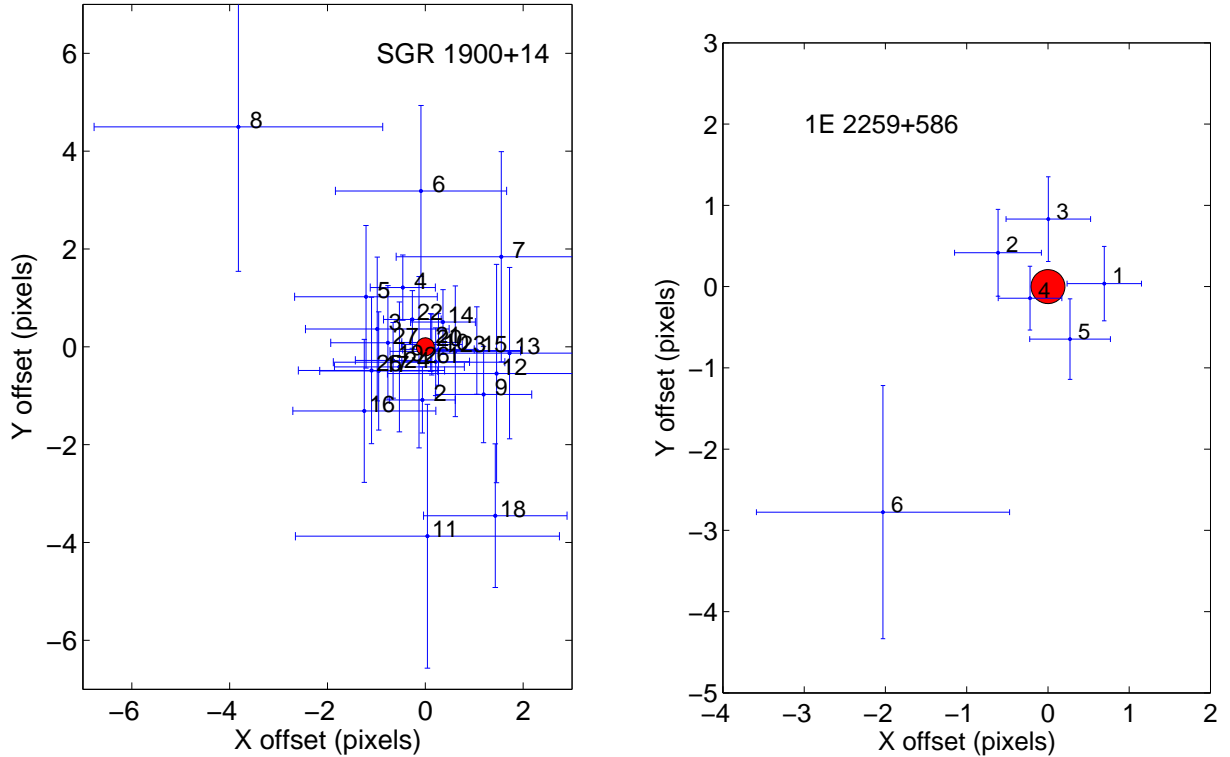


FIG. 7.— Residual position differences between epochs 2 and 1 reference sources used to compute the transformation for SGR 1900+14 (*Left*, with 27 reference sources) and 1E 2259+586 (*Right*, with 7 reference sources); the reference sources are labeled according to Tables 2 and 3. The differences plotted are the residuals left after fitting for 2-parameter (i.e., shift only) transformations. The filled circles at the centers show the uncertainty on the resulting transformations, which in this case is the uncertainty on the mean of the residuals.

TABLE 4
PROPER MOTION MEASUREMENTS FOR SGR 1900+14 AND 1E 2259+586

Parameter	SGR 1900+14		1E 2259+586	
	2-parameter	3-parameter	2-parameter	3-parameter
Transform χ^2/DOF	37.8/52	37.7/51	14.1/10	13.1/9
$(\Delta x, \Delta y)$ (pixels) ^a	$(0.02 \pm 0.19, 0.26 \pm 0.19)$	$(0.02 \pm 0.27, 0.26 \pm 0.27)$	$(-0.14 \pm 0.25, -0.45 \pm 0.25)$	$(-0.15 \pm 0.33, -0.39 \pm 0.34)$
(μ_x, μ_y) (mas yr ⁻¹) ^b	$(2 \pm 18, 26 \pm 18)$	$(2 \pm 26, 26 \pm 26)$	$(-11 \pm 20, -35 \pm 20)$	$(-11 \pm 26, -31 \pm 26)$
$\hat{\mu}$ (mas yr ⁻¹) ^c	26	26	36	32
$\langle \mu \rangle$ (mas yr ⁻¹) ^d	33	39	42	44
μ_{90} (mas yr ⁻¹) ^e	54	69	65	73
$\langle v_{\perp} \rangle$ (km s ⁻¹) ^f	$780d_5$	$930d_5$	$600d_3$	$630d_3$
$v_{\perp,90}$ (km s ⁻¹) ^g	$1300d_5$	$1600d_5$	$930d_3$	$1000d_3$

^a Shift in pixels between epochs.

^b Proper motion in the $(x_{\text{sky}}, y_{\text{sky}})$ frame between epochs.

^c Magnitude of the proper motion, computed from $\sqrt{\mu_x^2 + \mu_y^2}$.

^d Mean of the magnitude of the proper motion, from the distribution in Eqn. 3.

^e 90% upper limit to the magnitude of the proper motion, from the distribution in Eqn. 3.

^f Transverse velocity corresponding to $\langle \mu \rangle$, the mean of the magnitude of the proper motion, assuming a distance of $5d_5$ kpc (SGR 1900+14) or $3d_3$ kpc (1E 2259+586).

^g Transverse velocity corresponding to the μ_{90} , the 90% upper limit on the proper motion, assuming a distance of $5d_5$ kpc (SGR 1900+14) or $3d_3$ kpc (1E 2259+586).

disagreed by $\approx 3\sigma$ between the two epochs). While formally enough to determine a robust transformation, this is fewer than we might like to have. One problem here is that we are using ACIS-S, which has a smaller field of view. Here 1E 2259+586 is close to the center of a CCD (ACIS-S3), and we used sources from both ACIS-S3 and ACIS-S2. We chose to do the second epoch observation with ACIS-S as well, to best reproduce the first. There were some slight problems, though. As the roll angle

changed by 121° , the position of ACIS-S2 changed relative to the aim-point. Therefore, some of the reference sources detected in the first epoch were missed entirely by the detector in the second epoch, and vice versa. This also explains why some of the reference sources have such drastically different count-rates between the two epochs: some of them move from the front-illuminated (and hence less sensitive) ACIS-S2 to the back-illuminated ACIS-S3, although in other cases the difference in count-rate

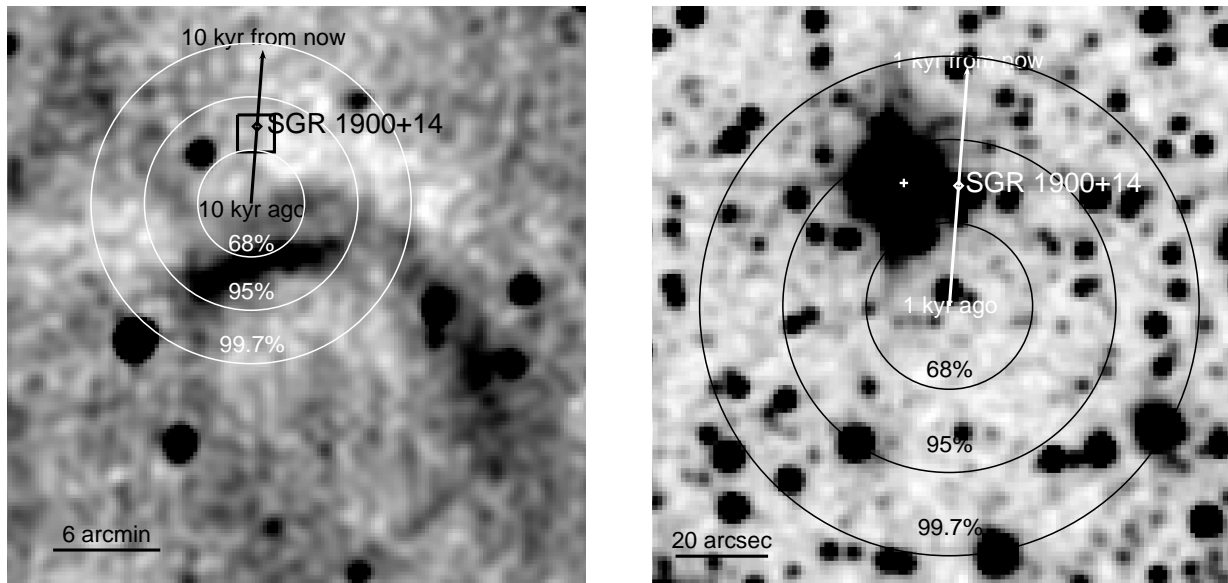


FIG. 8.— *Left*: Radio image of the field around SGR 1900+14 (Frail, Kulkarni, & Bloom 1999; marked with a diamond), showing SNR G42.8+0.6 (to the south of SGR 1900+14). The image is a 332 MHz image from Kaplan et al. (2002). The arrow shows the distance that SGR 1900+14 has moved, starting 10 kyr ago and projecting the same time into the future using our best-fit proper motion from Table 4. We also show 1-, 2-, and 3- σ error circles (68%, 95%, and 99.7% confidence) on the position 10 kyr ago. *Right*: the same but plotted on a near-infrared ($2.2 \mu\text{m}$) image from the Two Micron All Sky Survey (2MASS; Skrutskie et al. 2006). The position of the cluster found by Vrba et al. (2000) is marked with a cross. The scale of this image is reduced by a factor of ~ 10 from the radio image (the box on the radio image is the field shown in the near-IR image), as the proper motion vector now only shows the distance that SGR 1900+14 has moved/will move over 1 kyr. There are scale bars in the lower left corners, and the images have north up and east to the left.

is intrinsic, and may reflect flare stars or other variable sources.

We computed 2- and 3-parameter transformations. As with SGR 1900+14, the 3-parameter transformation did not provide any improvement. With the 2-parameter transformation, we find the position residuals in Figure 7. We also repeated the jackknife and bootstrap tests (§ 4). The residuals in Figure 7 show an outlier, but it is relatively minor and the jackknifed transformations are consistent with the mean.

With the transformations from the six reference sources, we again find only an upper limit to a displacement between the two epochs: $\mu < 65 \text{ mas yr}^{-1}$ at 90% confidence (translating to $v_{\perp} < 930 d_3 \text{ km s}^{-1}$), with additional details given in Table 4. Unlike SGR 1900+14, where the reduced χ^2 for the 2-parameter transformation was less than 1.0, here it is 1.4. This appears slightly worrisome, and could indicate that we have underestimated our uncertainties, which would make the inferred proper motion less significant. However, the majority of the problem is caused by a single source, #6 in Table 3. This source deviates by $\approx 1.5\sigma$, and without it the reduced χ^2 becomes 1.1. Including source #6, it is still not impossible to get such a large reduced χ^2 even with a proper description of the data: it should happen about 17% of the time, so our result is not really surprising (also recall that our tests with the HDF-N observations gave a reduced χ^2 of 1.33 for 1450 DOF with the ChaMP model). Overall, the residuals for the remaining sources are reasonably well behaved, and given the tests for SGR 1900+14 and those in § 3.1, we believe that our uncertainties are on the whole reliable.

4.3. Prospects for Improvement

Our result here is formally a non-detection of the proper motions of SGR 1900+14 and 1E 2259+586.

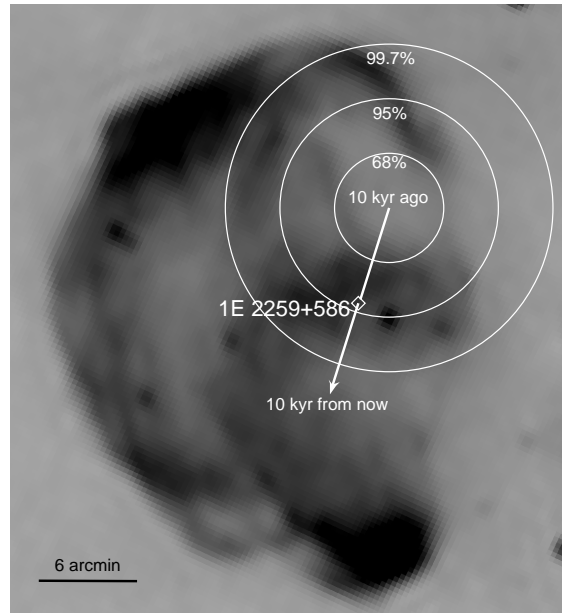


FIG. 9.— Radio image of the SNR CTB 109 at 1.4 GHz, with the position of 1E 2259+586 marked. The image is from the Canadian Galactic Plane Survey (CGPS; Taylor et al. 2003). The diamond shows the current position of 1E 2259+586 (Hulleman et al. 2001). The arrow shows the distance that 1E 2259+586 has moved, starting 10 kyr ago and projecting the same time into the future using our best-fit proper motion from Table 4. We also show 1-, 2-, and 3- σ error circles (68%, 95%, and 99.7% confidence) on the position 10 kyr ago. The scale bar in the lower left indicates $6'$, and the image has north up and east to the left.

However, the direction and magnitude of SGR 1900+14 are suggestive, pointing as they do to a nearby SNR (see § 5). It would therefore be interesting to confirm or refute our measurements with newer data. Beyond this, one must always view 2-point proper motions with suspicion, as a line can always be fit to two points, and

only with the inclusion of a third observation does one begin to gain confidence in the result. The biggest limiting factor is astrometry of the reference sources (this is similar to what was found by Motch et al. 2007a,b): increasing the number or accuracy of those measurements would be ideal, but that would have to be done for all of the observations. Just improving the newest one would have little impact. If we assume similar observations to those presented here, we can achieve frame matching to a precision of ≈ 0.2 pixels between a pair of observations. To measure a proper motion of the order of $\sim 26 \text{ mas yr}^{-1}$, we would need to wait > 10 yrs from the first observation for a statistically significant ($> 3\sigma$) measurement. This is only considering the first and last data-sets, though: by analyzing all three observations together we can establish a more robust reference frame and confirm the measurement of displacement. Regardless, we would need to wait until 2010 or so before this will be possible. Observations at other wavelengths, possible for 1E 2259+586 at least, should be able to achieve higher precision (Cameron et al. 2008, P. B. Cameron 2008, pers. comm.).

Another approach would be to use the High Resolution Camera (HRC; Murray et al. 1997) on *Chandra*. The pixel scale is almost factor of four smaller than that of ACIS, so the HRC has the potential for better spatial resolution. However, the effective resolution is $\approx 0''.5$, not that different from ACIS. It also does not suffer from pileup, so bright sources can be observed without penalty. The main drawback is that because of lower overall efficiency few, if any, reference sources are detected: Hui & Becker (2006) and Winkler & Petre (2007) found only two and three sources, respectively. The accuracy of our present work is limited by the registration of the separate observations which depends on the reference sources. This was true even for 1E 2259+586, where pileup limited the centroiding accuracy. Even so, Winkler & Petre (2007) found a significant proper motion of $165 \pm 25 \text{ mas yr}^{-1}$ for RX J0822–4300 using three HRC observations (also see Hui & Becker 2006 for an earlier but consistent result).

5. DISCUSSION AND CONCLUSIONS

Our proper motion limit can be used to limit the age of SGR 1900+14/SNR G42.8+0.6, assuming an association. From the 327-MHz radio data from Kaplan et al. (2002), we represent SNR G42.8+0.6 as a ring centered at (J2000): $\alpha = 19^{\text{h}}06^{\text{m}}59^{\text{s}}.4$, $\delta = +09^{\circ}03'05''$, and with a radius of $\approx 9.5'$ (see Fig. 8). SGR 1900+14 would have needed > 16 kyr to traverse the separation of $15'$, using the 90% confidence upper limit on the proper motion. This is not a remarkably large age for a magnetar (Gaensler et al. 2001; Woods & Thompson 2006). Suggestively, the marginal proper motion that we find is directed to the north, and SGR 1900+14 sits beyond the northern rim of SNR G42.8+0.6. However, our proper motion is so uncertain in both direction and magnitude that an association between SGR 1900+14 and the cluster found by Vrba et al. (2000) is also consistent with the data.

For 1E 2259+586, we find an upper limit to the proper motion. The SNR CTB 109 (see Fig. 9), with which 1E 2259+586 is generally taken to be associated, has a somewhat complicated morphology (Kothes et al.

2002) with what may be multiple shells and seems to be interacting with a giant molecular cloud to the west (Tatematsu et al. 1990). The site of the explosion is not particularly well defined, given the different shells and the impeded expansion to the west. However, there does not appear to be any suggestion that 1E 2259+586 is displaced to the south relative to the explosion center, as our proper motion limit might suggest. The magnitude of the proper motion limit is not huge: for an age of $1000t_3$ yr, 1E 2259+586 would have moved $1t_3$ arcmin, so it could have still had an origin within the current $\approx 30'$ -diameter shell for ages up to $t_3 \sim 10$. Therefore our data do not greatly constrain the association between 1E 2259+586 and CTB 109 (generally assumed to be secure).

Taken together, we can try to use the velocities we measure/limit to understand if magnetars have a velocity distribution comparable to that of the radio pulsar population. The proper motion of XTE J1810–197 (Helfand et al. 2007) and the velocity limits inferred by Gaensler et al. (2001) are less than 500 km s^{-1} . For the magnetars considered here, though our results are less constraining. This is made worse by the very uncertain distances to these objects. If we accept the association between SGR 1900+14 and the massive star cluster of Vrba et al. (2000, also see Wachter et al. 2008), then we must also accept a distance to SGR 1900+14 of ≈ 15 kpc. This means that our 90% upper limit on the transverse velocity is 3800 km s^{-1} , which encompasses the extreme range of velocities posited for the magnetars (e.g., Duncan & Thompson 1992; Thompson & Duncan 1993, 1995), but the fact of the association itself would imply a small proper motion on the order of $\sim 5 \text{ mas yr}^{-1}$. For 1E 2259+586, our transverse velocity limit is moderately constraining (although with the larger distance of Durant & van Kerkwijk 2006 it increases to almost 2500 km s^{-1}).

Future astrometric observations will help answer some of these questions. We now understand in detail what the limiting factors are, and a third epoch of data around 2010 should allow definitive measurement of the proper motions presented here. However, the velocity situation will remain more uncertain, owing to the factor of 3 uncertainty in the distance to SGR 1900+14 as well as unknown projection effects.

Support for this work was provided by the National Aeronautics and Space Administration through *Chandra* award GO6-7066X. Partial support for DLK was also provided by NASA through Hubble Fellowship grant #01207.01-A awarded by the Space Telescope Science Institute, which is operated by the Association of Universities for Research in Astronomy, Inc., for NASA, under contract NAS 5-26555. B.M.G. acknowledges the support of a Federation Fellowship from the Australian Research Council through grant FF0561298. Support for SC was provided by the University of Sydney Postdoctoral Fellowship program. POS also acknowledges support from NASA contract NAS8-201039073. The research presented in this paper has used data from the Canadian Galactic Plane Survey, a Canadian project with international partners, supported by the Natural Sciences and Engineering Research Council.

REFERENCES

- Cameron, P. B., Britton, M. C., & Kulkarni, S. R. 2008, *AJ*, submitted, arXiv:0805.2153
- Carter, C., Karovska, M., Jerius, D., Glotfelty, K., & Beikman, S. 2003, in *Astronomical Society of the Pacific Conference Series*, Vol. 295, *Astronomical Data Analysis Software and Systems XII*, ed. H. E. Payne, R. I. Jedrzejewski, & R. N. Hook (San Francisco: ASP), 477
- Chatterjee, S., et al. 2005, *ApJ*, 630, L61
- Duncan, R. C. & Thompson, C. 1992, *ApJ*, 392, L9
- Durant, M. & van Kerkwijk, M. H. 2006, *ApJ*, 650, 1070
- Efron, B. & Tibshirani, R. J. 1993, *An Introduction to the Bootstrap* (London: Chapman and Hall)
- Fahlman, G. G. & Gregory, P. C. 1981, *Nature*, 293, 202
- Frail, D. A., Kulkarni, S. R., & Bloom, J. S. 1999, *Nature*, 398, 127
- Freeman, P. E., Kashyap, V., Rosner, R., & Lamb, D. Q. 2002, *ApJ*, 559, 963
- Gaensler, B. M., McClure-Griffiths, N. M., Oey, M. S., Haverkorn, M., Dickey, J. M., & Green, A. J. 2005, *ApJ*, 620, L95
- Gaensler, B. M., Slane, P. O., Gotthelf, E. V., & Vasisht, G. 2001, *ApJ*, 559, 963
- Garmire, G. P., Bautz, M. W., Ford, P. G., Nousek, J. A., & Ricker, G. R. 2003, *Proc. SPIE*, 4851, 28
- Gavriil, F. P., Gonzalez, M. E., Gotthelf, E. V., Kaspi, V. M., Livingstone, M. A., & Woods, P. M. 2008, *Science*, 319, 1802
- Gotthelf, E. V., Halpern, J. P., Buxton, M., & Baily, C. 2004, *ApJ*, 605, 368
- Halpern, J. P., Gotthelf, E. V., Becker, R. H., Helfand, D. J., & White, R. L. 2005, *ApJ*, 632, L29
- Helfand, D. J., Chatterjee, S., Brisken, W. F., Camilo, F., Reynolds, J., van Kerkwijk, M. H., Halpern, J. P., & Ransom, S. M. 2007, *ApJ*, 662, 1198
- Hobbs, G., Lorimer, D. R., Lyne, A. G., & Kramer, M. 2005, *MNRAS*, 360, 974
- Hong, J., van den Berg, M., Schlegel, E. M., Grindlay, J. E., Koenig, X., Laycock, S., & Zhao, P. 2005, *ApJ*, 635, 907
- Hornschemeier, A. E., et al. 2000, *ApJ*, 541, 49
- Hui, C. Y. & Becker, W. 2006, *A&A*, 457, L33
- Hulleman, F., Tennant, A. F., van Kerkwijk, M. H., Kulkarni, S. R., Kouveliotou, C., & Patel, S. K. 2001, *ApJ*, 563, L49
- Hurley, K., et al. 1999a, *Nature*, 397, 41
- Hurley, K., Kouveliotou, C., Woods, P., Cline, T., Butterworth, P., Mazets, E., Golenetskii, S., & Frederics, D. 1999b, *ApJ*, 510, L107
- Hurley, K., et al. 1999c, *ApJ*, 510, L111
- Hurley, K., et al. 1996, *ApJ*, 463, L13
- Kaplan, D. L., Kulkarni, S. R., Frail, D. A., & van Kerkwijk, M. H. 2002, *ApJ*, 566, 378
- Kaplan, D. L., van Kerkwijk, M. H., & Anderson, J. 2007, *ApJ*, 660, 1428
- Kaspi, V. M. & McLaughlin, M. A. 2005, *ApJ*, 618, L41
- Kasumov, F. K., Allakhverdiev, A. O., & Asvarov, A. I. 2006, *Astronomy Letters*, 32, 308
- Kim, M., et al. 2007, *ApJS*, 169, 401
- Kothes, R., Uyaniker, B., & Yar, A. 2002, *ApJ*, 576, 169
- Kouveliotou, C., et al. 1994, *Nature*, 368, 125
- Kouveliotou, C., et al. 1999, *ApJ*, 510, L115
- Kulkarni, S. R., Kaplan, D. L., Marshall, H. L., Frail, D. A., Murakami, T., & Yonetoku, D. 2003, *ApJ*, 585, 948
- Lai, D. 2001, in *Lecture Notes in Physics*, Vol. 578, *Physics of Neutron Star Interiors*, ed. D. Blaschke, N. K. Glendenning, & A. Sedrakian (Berlin: Springer Verlag), 424
- Lampton, M., Margon, B., & Bowyer, S. 1976, *ApJ*, 208, 177
- Lin, J. R. & Zhang, S. N. 2004, *ApJ*, 615, L133
- Lorimer, D. R. & Xilouris, K. M. 2000, *ApJ*, 545, 385
- Mazets, E. P., Golenetskij, S. V., & Guryan, Y. A. 1979, *Soviet Astronomy Letters*, 5, 343+
- Mereghetti, S., et al. 2006, *ApJ*, 653, 1423
- Motch, C., Pires, A. M., Haberl, F., & Schwöpe, A. 2007a, *Ap&SS*, 69
- Motch, C., Pires, A. M., Haberl, F., Schwöpe, A., & Zavlin, V. E. 2007b, in *40 Years of Pulsars: Millisecond Pulsars, Magnetars and More*, Vol. 712, arXiv:0712.0342
- Muno, M. P., et al. 2006, *ApJ*, 636, L41
- Murray, S. S. et al. 1997, *Proc. SPIE*, 3114, 11
- Ng, C.-Y. & Romani, R. W. 2007, *ApJ*, 660, 1357
- Paczynski, B. 1992, *Acta Astronomica*, 42, 145
- Papoulis, A. 1991, *Probability, random variables and stochastic processes*, 3rd edn. (New York: McGraw-Hill)
- Patel, S. K., et al. 2001, *ApJ*, 563, L45
- Rothschild, R. E., Kulkarni, S. R., & Lingenfelter, R. E. 1994, *Nature*, 368, 432
- Skrutskie, M. F., et al. 2006, *AJ*, 131, 1163
- Tatematsu, K., Fukui, Y., Iwata, T., Seward, F. D., & Nakano, M. 1990, *ApJ*, 351, 157
- Taylor, A. R., et al. 2003, *AJ*, 125, 3145
- Thompson, C. & Duncan, R. C. 1993, *ApJ*, 408, 194
- . 1995, *MNRAS*, 275, 255
- . 1996, *ApJ*, 473, 322
- Vasisht, G., Kulkarni, S. R., Frail, D. A., & Greiner, J. 1994, *ApJ*, 431, L35
- Vrba, F. J., Henden, A. A., Luginbuhl, C. B., Guetter, H. H., Hartmann, D. H., & Klose, S. 2000, *ApJ*, 533, L17
- Wachter, S., Ramirez-Ruiz, E., Dwarkadas, V. V., Kouveliotou, C., Granot, J., Patel, S. K., & Figer, D. 2008, *Nature*, 453, 626
- Winkler, P. F. & Petre, R. 2007, *ApJ*, 670, 635
- Woods, P. M. & Thompson, C. 2006, in *Compact stellar X-ray sources*, ed. W. Lewin & M. van der Klis (Cambridge, UK: Cambridge University Press), 547
- Zhang, B. & Harding, A. K. 2000, *ApJ*, 535, L51